CrossMark

Structural, dielectric and magnetic characteristics of Bi(Ni$_{0.25}$Ti$_{0.25}$Fe$_{0.50}$)O$_3$ ceramics

Alok Shukla[1] · Nitin Kumar[1] · C. Behera[2] · R. N. P. Choudhary[2]

Abstract The polycrystalline sample of Bi(Ni$_{0.25}$Ti$_{0.25}$Fe$_{0.50}$)O$_3$ was synthesized using a standard high-temperature solid-state reaction technique. Room temperature structural analysis of the above material, carried out using X-ray diffraction data, shows the formation of a single-phase compound with orthorhombic structure which is different from that of its parent compound (BiFeO$_3$). The co-substitution of Ni^{2+} and Ti^{4+} at the Fe^{3+}-site of BiFeO$_3$ enhances its dielectric, ferroelectric and magnetic properties with significant reduction of electrical leakage current or tangent loss. Room temperature surface morphology and texture of the samples, recorded by a field-emission scanning electron microscope, reveal the uniform distribution of grains on the surfaces of the sample. Studies of dielectric, modulus and impedance spectroscopy on (Ni, Ti) modified BiFeO$_3$ over a wide frequency (1 kHz–1 MHz) and temperature (25–500 °C) ranges provide many interesting features of the material useful for devices. Impedance and modulus plots were used as tools to analyze the sample behavior as a function of frequency. Cole–Cole plots showed a non-Debye relaxation.

1 Introduction

Recent years have witnessed enormous interest in multiferroic materials which have attracted a lot of attention due to their potential applications in memory devices, spintronic devices, magnetically modulated transducers, ultrafast optoelectronic devices, sensors and so on [1–4]. BiFeO$_3$ (BFO) is now the most studied compound which has ferroelectric as well as G-type anti-ferromagnetic orderings much above room temperature (T$_c$ = 810–830 °C and T$_N$ = 350–370 °C) [5]. The room temperature crystal structure of polar phase of BFO is better described by rhombohederally-distorted perovskite structure with R3c space group. The structural distortion in the rhombohedral phase can be described in terms of the anti-phase tilting of the adjacent oxygen octahedra (a$^-$ a$^-$ a$^-$ tilt system in Glazer's notation [6]) with respect to ideal perovskite, and the polar ionic displacements along the $\langle 111 \rangle_{cubic}$ direction of the parent cubic cell ([0 0 1]$_{hex}$ direction in the hexagonal setting). In BFO, ferroelectric properties is due to the presence of 6 s lone pair electrons of Bi^{+3} ions, and thus ferromagnetic order is due to Fe^{+3} ions [7]. Unfortunately, the major problems of BFO and other members of this family are their high-leakage current density, high tangent loss, structural distortion etc., which affect the values of dielectric, ferroelectric and resistive properties. The high-leakage current of BiFeO$_3$ (BFO) is attributed to the oxidation–reduction of Fe ions (Fe^{+2} → Fe^{+3} + e$^-$), creating oxygen vacancies for charge compensation [8, 9].

Nickel titanate (NiTiO$_3$) belongs to ilmenite family of a general formula; ATiO$_3$ (A = Fe, Ni, Sr, Ba, Co). Some members of this family have been found interesting and important because of their wide range of applications in photo-catalysis, sensor, fuel cell, high temperature superconductor, etc. [10–15]. NiTiO$_3$ has also centro-symmetry rhombohedral structure [16–18] where both Ni and Ti

✉ Nitin Kumar
 nitinphysicskushawaha@gmail.com

[1] Department of Physics, National Institute of Technology Mizoram, Aizawl 796012, India

[2] Multifunctional Materials Research Laboratory, Department of Physics, ITER, SOA University, Bhubaneswar, Odisha 751030, India

atoms prefer octahedral coordination with alternating cation layers solely occupied by either Ni or Ti [19] or both. Though various methods have been attempted to develop materials with multiferroic with high order of coupling, one of the suitable approaches is to combine different kinds of ferroic materials. As nickel titanate ($NiTiO_3$) exhibits ferroelectric with excellent electrical properties, it has been modified to $Bi(NiTi)O_3$ by adding bismuth oxide in it to provide more useful properties for devices. In order to solve some of the above inherent problems of multiferroics, an attempt has been made to synthesis titled compound with $BiFeO_3$ and $Bi(Ni_{0.5}Ti_{0.5})O_3$ in equal mole-ratio on which not much works have been reported so far. In the present paper we report synthesis and characterisation (structural, dielectric, impedance, and magnetic properties) of (Ni, Ti)-substituted bismuth ferrite [i.e., $Bi(Ni_{0.25}Ti_{0.25}Fe_{0.50})O_3$].

2 Materials and methods

The polycrystalline (ceramic) sample of a chemical composition; $Bi(Ni_{0.25}Ti_{0.25}Fe_{0.50})O_3$ (BNTF) was prepared by a standard solid-state reaction technique using high-purity (>99.5 %) carbonate and oxides such as; bismuth carbonate [$(BiO)_2CO_3 \cdot H_2O$], nickel oxide [NiO], iron oxide [Fe_2O_3] and titanium dioxide [TiO_2] in a suitable stoichiometric ratio. These ingredients were first thoroughly mixed by using agate mortar and pestle in dry medium (air) for 8 h, and then in wet medium (methanol) for 10 h. The homogeneous mixture of the ingredients was calcined at an optimised temperature (750 °C) and time (6 h). The formation of single phase of calcined powder of BNTF (at room temperature) and basic crystal data were studied by experimental data collected by powder X-ray diffraction (Rigaku Diffractometer, Japan) with CuKα radiation ($\lambda = 1.5405$ Å) in a wide range of Bragg angles ($20° \leq 2\theta \leq 70°$) at a scan speed of $2°$ m^{-1}. The microstructural characteristics of the sample were investigated by using field emission scanning electron microscope (FE-SEM, EVO HD 15 Carl Zeiss). The calcined powder of the material was cold pressed into circular disc-shaped pellets (10 mm diameter and 1–2 mm thickness) at the pressure of 5×10^6 N m^{-2} (with PVA as binder) by using a hydraulic press. The PVA burnt out during high-temperature sintering. The prepared pellets were then sintered at an optimized temperature of 800 °C for 6 h in air atmosphere. The sintered pellets were then polished with fine emery paper to make their surfaces smooth and parallel for electric measurements. Finally, the opposite faces of a pellet sample was coated with high-purity conducting silver paint (Alfa Aesar) and dried at 150 °C for 4 h to remove the moisture from the sample prior to electrical measurements.

The capacitance (C_p), impedance (Z), dielectric constant (ε_r), loss tangent (tan δ), electric modulus (M) and other related parameters were measured as a function of temperature (25–500 °C) over a wide range of frequency (1 kHz–1 MHz) using a computer-interfaced phase sensitive meter (N4L PSM, Model 1735, UK) and a laboratory-fabricated sample holder. For understanding of the magnetic properties of the prepared sample, M–H loop of the un-silvered pellet was measured with the help of vibrating sample magnetometer (VSM, Lake Shore, Model 7410).

3 Results and discussion

3.1 Structural and microstructural analyses

Figure 1 shows the XRD pattern of BNTF. The presence of some small peaks suggests that the material contains some impurity phases, such as, $Bi_2Fe_4O_9$ and $Bi_{25}FeO_{40}$ which are normally observed in XRD pattern of bismuth ferrite [20]. The diffraction pattern consists of a number of sharp and small peaks. Most of the prominent peaks of the patterns are equivalent to the perovskite structure but different from those of the ingredients, and thus confirming the formation of new polycrystalline phase of the compound. The XRD pattern of BNTF powder exhibits splitting of the higher angle peaks confirming the existence of orthorhombic phase of the materials.

The Goldschmidt tolerance factor (t) of $BiFeO_3$ structure is defined as,

$$t = \frac{(\langle r_A \rangle + r_o)}{\sqrt{2}(\langle r_B \rangle + r_o)} \tag{1}$$

Here $\langle r_A \rangle$ and $\langle r_B \rangle$ is the average radius of A and B site cations respectively and r_o is the ionic radius of oxygen.
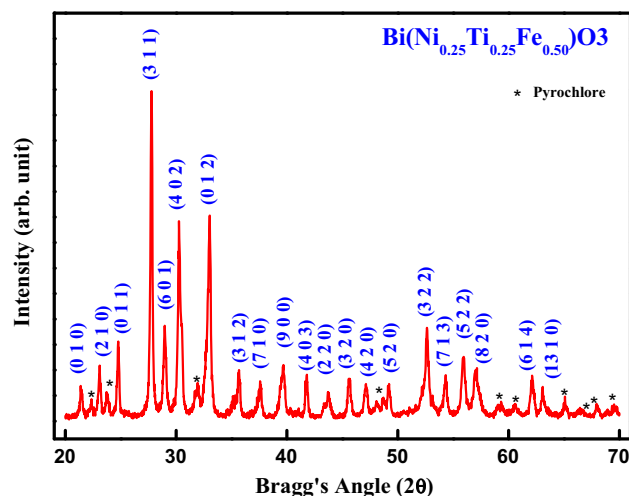

Fig. 1 Room temperature XRD pattern of the calcined powder of $Bi(Ni_{0.25}Ti_{0.25}Fe_{0.50})O_3$

The tolerance factor is used to quantify the structural stability of perovskite compounds. The value of t is 1 for an ideal cubic structure. When the value of "t" is smaller than one, the compressive strain acts on the Fe–O bonds, and hence on Bi–O bond which infers that the oxygen octahedral must buckle in order to at a bigger cation into a smaller space for minimum lattice strain.

A standard software 'POWDMULT' was used to index all the peaks [21] in different crystal systems. Based on the best agreement between observed (obs.) and calculated (cal.) inter planar spacing d [(i.e., $\sum \Delta d = d_{obs.} - d_{cal.}$ = minimum)], unit cell (lattice) parameters and volume of BNTF the compound were determined and hence system was found to be orthorhombic. The selected lattice parameters were refined using least-squares refinement sub-routine of the above computer software. The refined lattice parameters are: a = 20.4677 Å, b = 4.1505 Å, c = 7.1446 Å (with ±0.004 as minimum standard deviation) and volume V = 606.94 Å^3. By using strong reflection peak (3 1 1) of XRD pattern, the crystallite size of the sample was calculated to be 39 nm from the broadening of reflections using Scherrer's formula [22, 23] which is defined as D = kλ/β Cos θ. In this equation, constant k depends upon the shape of the crystallite size (= 0.89, assuming the spherical crystallites), β = full width at half maximum (FWHM) of intensity versus 2θ plot, λ is the wavelength of the Cu Kα radiation (= 1.5418 Å), θ is the Bragg's diffraction angle and D is the crystallite size. The average crystallite size of the prepared compound (28 nm) is somehow higher but comparable to that of reported one for semiconductor nano-particles [24].

Figure 2 exhibits the room temperature field emission scanning electron (FE-SEM) micrograph of the sintered pellet. It is clear from the micrograph that the grains are densely packed with very few voids, and are uniformly distributed throughout the surface of the sample. The grains are of different shape and size indicating the existence of polycrystalline microstructure. They are of unequal sizes but with distinct grain boundaries. The average grain size is estimated to be 100–400 nm. The difference in structural parameters is because crystallites are different from their grain size. The XRD is for the bulk study whereas SEM is for a surface study. Therefore, XRD gives crystallite (particle) size whereas SEM gives the grain size.

3.2 Dielectric properties

Figure 3a, b shows variation of relative dielectric constant (ε_r) and corresponding tangent loss (tan δ) as a function of temperature at various selected frequencies (1, 25, 50, 100, 500 and 1000 kHz). The observed values of dielectric constant have several significant contributions such as, (1)
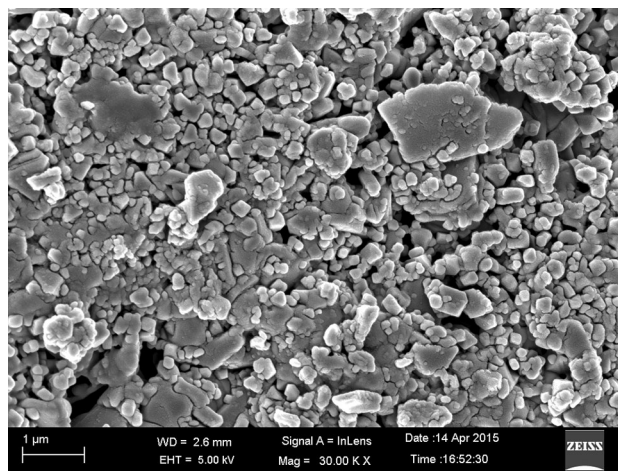

Fig. 2 FE-SEM micrograph of $Bi(Ni_{0.25}Ti_{0.25}Fe_{0.50})O_3$ ceramics at room temperature
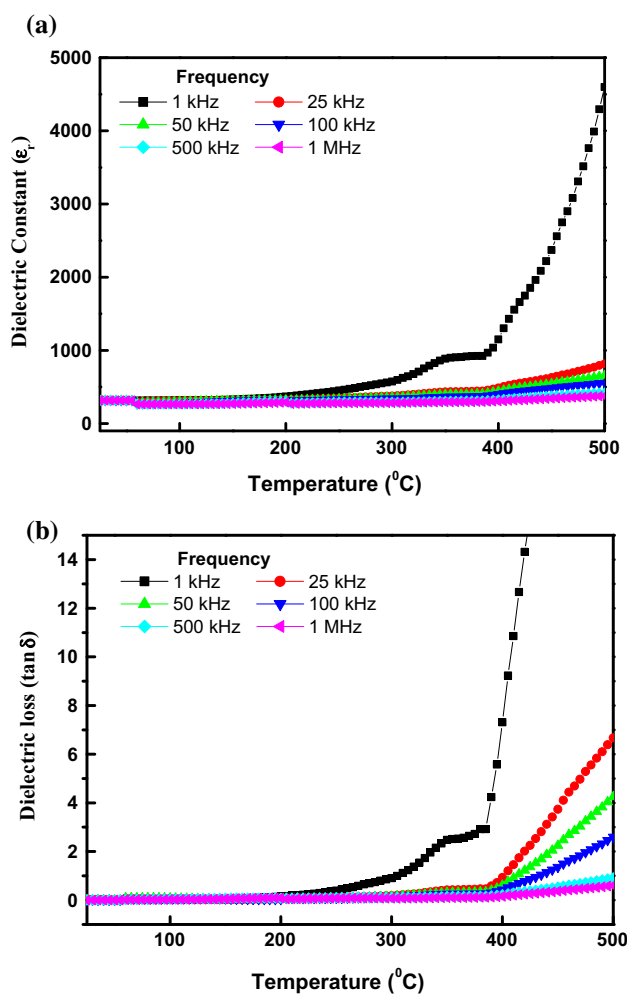

Fig. 3 a Variation of dielectric constant (ε_r) as a function of temperature of BNTF sample at different frequencies. **b** Variation of dielectric loss (tan δ) as a function of temperature of BNTF sample at different frequencies

decrease in the oxygen vacancies where impurity phases increase the dielectric constant, (2) Ni and Ti substitution turn off the lone-pair activity of Bi^{3+} ($6s^2$) responsible for the ferroelectric distortion which in turn reduces the dipolar contribution in dielectric constant; (3) crystallographic phase competition between two crystal symmetries increases the dielectric constant due to enhanced strain; and (4) increase in phase fraction of orthorhombic crystal symmetry (Pbnm space group) decreases the contribution of dipolar-polarization in dielectric constant. The value of ε_r increases on increasing temperature. This increase in the value of ε_r can be due to the electron–phonon interaction, which is mainly observed in niobates, and many other related compounds [25, 26]. The observed higher value of dielectric constant at lower frequency is due to the charge accumulation at grain boundaries [27]. The value of ε_r (Fig. 3a) at 1 kHz at room temperature (RT) and 500 °C are 334 and 4669 respectively. The increase in the value of ε_r can be ascribed to the thermally activated transport of space charges. The figure shows that both the dielectric parameters (ε_r and tan δ) decrease on increasing frequency, which is a general feature of dielectric materials [28].

In addition, the value of dielectric loss (tan δ) at 1 kHz at RT and 500 °C are 0.017 and 26 respectively. No phase transition is observed in the experimental temperature range of (25–500 °C). The nature of variation of tan δ with temperature (Fig. 3b) is same as that of ε_r (i.e., the value of tan δ gradually increases on increasing temperature). Generally, tan δ has very high value in low-frequency and high-temperatures range in Fe containing compounds which decreases rapidly with rise in frequency.

3.3 Impedance spectrum analysis

The impedance spectroscopy (IS) based on analyzing the ac response of a system to a sinusoidal perturbation, and subsequent calculation of impedance and related parameters as a function of frequency at different temperatures [29–33]. The various impedance parameters of materials (i.e., capacitive and resistive components), represented by the Nyquist plot, lead to a succession of semicircles. The frequency dependence of dielectric properties of the materials is normally described in terms of complex dielectric constant ($\varepsilon* = \varepsilon' - j\varepsilon''$), complex impedance ($Z* = Z' - jZ'' = R_s - \frac{j}{\omega c_s}$), electric modulus ($M* = M' + jM'' = j\omega Co Z*$) and dielectric loss (tan $\delta = \frac{\varepsilon''}{\varepsilon'} = \frac{-Z'}{Z''} = \frac{M''}{M'}$) etc., are related to each other, where ω is the angular frequency, ε_0 is the permittivity in free space, R_s and C_s are resistance and capacitance in series respectively. The above expressions offer a wide scope for graphical representation as they can be used to calculate complex impedance of the electrode/

ceramic/electrode capacitor (demonstrated as the sum of the single RC circuit with parallel combination) as per the below relation:

$$Z*(T) = Z_0(T) \int \frac{Y(\tau,\, T)\, d(\tau)}{1 + j\,\omega\tau}$$

This complex equation can be resolved in real and imaginary part of Z*, and can be expressed as

$$Z'(\omega,\, T) = Z_0(T) \int \frac{Y(\tau,\, T)\, d(\tau)}{1 + \omega^2\tau^2}$$

$$Z''(\omega,\, T) = Z_0(T) \int \frac{(\omega\tau)*\, Y(\tau,\, T)\, d(\tau)}{1 + \omega^2\tau^2}$$

Here, $\tau = R_bC_b$ represents the relaxation time, T = time period and Y(τ, T) = distribution function of relaxation time. The variation of imaginary part of complex impedance Z'' (ω, T) provides information about the distribution function Y(τ, T).

Figure 4 shows the variation of real and imaginary part of impedance (Z' and Z'') of Bi(Ni$_{0.25}$Ti$_{0.25}$Fe$_{0.50}$)O$_3$ with frequency at different temperatures. The value of Z' decreases with rise in frequency, but increases with increase in temperature. The magnitude of Z' decreases on increasing temperature in the low-frequency range that merges in the high-frequency region irrespective of temperature. The nature of the plot may be due to the release of space charge [28]. The reduction in barrier properties of the materials with rise in temperature may be a responsible factor for enhancement of ac conductivity of the materials at higher frequencies [34, 35]. Further, in the low-frequency region, there is a decrease in magnitude of Z' with rise in temperature showing negative temperature coefficient of resistance (NTCR) behavior. This behaviour is changed drastically in the high-frequency region showing complete merger of Z' plot above a certain frequency. At
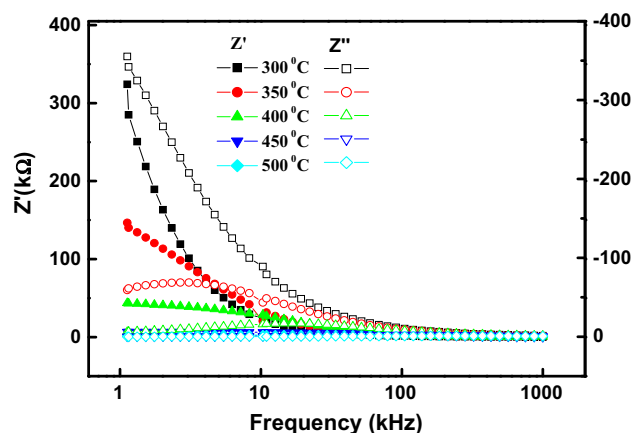

Fig. 4 Frequency and temperature dependent of Z' and Z'' for Bi(Ni$_{0.25}$Ti$_{0.25}$Fe$_{0.50}$)O$_3$ ceramics

high-frequency, the value of Z' of different temperature coincides implying the possible release of space charge [33]. A peak of a particular frequency (at which Z' becomes independent of frequency) was observed to shift towards the higher frequency side on increasing temperature. The shift in Z' plateau indicates the existence of frequency relaxation process in the material. The curves display single relaxation process and indicate the increase in ac conductivity with increase in temperature and frequency [34].

The loss spectrum of the material has a few important features, such as (1) a monotonous decrease in Z'' in the low-temperature region, (2) appearance of peaks in the loss spectrum at high temperatures, (3) significant increase in peak broadening with increase in temperature and (4) existence of symmetric peak broadening. The absence of peaks in the low-temperature range for the BNTF ceramics in the loss spectrum suggests the lack of current dissipation in this temperature region. The pattern shows peaks at a particular frequency that describes the type and strength of electrical relaxation phenomenon in the material [36]. The value of Z'' reaches a maximum peak (Z''_{max}) at 300 °C. The Z''_{max} shifts to higher frequency side on increasing temperature, indicating an increase of tangent loss in the sample. A significant increase in the broadening of the peaks with increase in temperature suggests the existence of a temperature dependence of electrical relaxation phenomenon in the material. The relaxation process may be due to the presence of electrons/immobile species at low temperatures and defects/vacancies at higher temperatures. The asymmetric broadening of the peaks suggests a spread of relaxation time with two equilibrium positions. The peak height is proportional to bulk resistance (R_b), and can be estimated and explained by the equation, $Z''[= R_b\{\omega\tau/(1+\omega^2\tau^2)\}]$ in Z'' versus frequency plots. Further, the magnitude of Z'' decreases gradually with a shift in peak frequency towards higher frequency side, and it finally merges in the high-frequency region. This is an indication of the accumulation of space charge in the material [37].

It is observed that with increase in temperature, both Z' and Z'' decrease. The value of Z''_{max} shifts to higher frequency side on increasing temperature of the material indicating an increase of tangent loss. A significant increase in the broadening of the peaks with increase in doping concentration suggests the enhancement in electrical relaxation phenomenon in the material.

Figure 5a shows complex impedance spectrum of the BNTF ceramics obtained at different temperatures over a wide range of frequency (100 Hz–1 MHz). The impedance properties of the material are characterized by the formation of semicircular arcs whose pattern of evolution
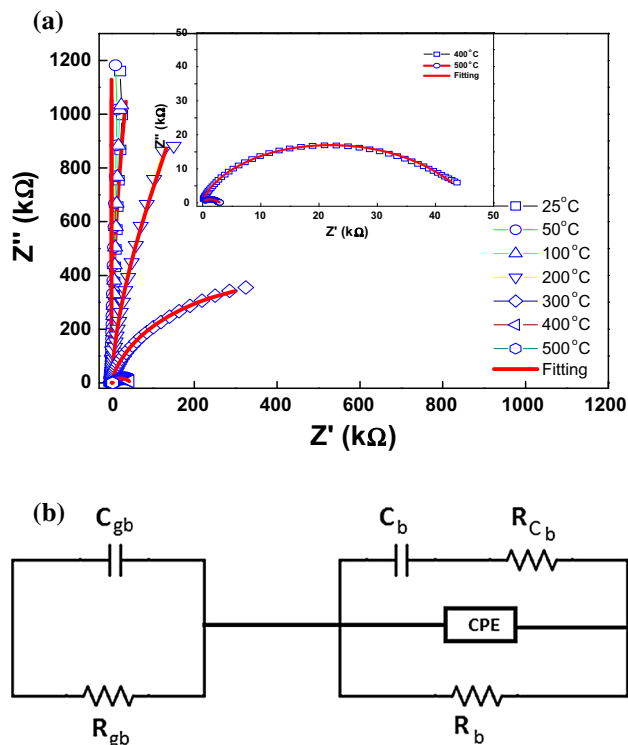

Fig. 5 a Variation of Z' with Z'' (Nyquist plots) of $Bi(Ni_{0.25}Ti_{0.25}Fe_{0.50})O_3$ at selected temperatures. **b** Equivalent circuit for Nyquist plots

changes with change in temperature. The extent of intercept of semicircles on the real axis (x-axis) and its number in the spectrum provide information on the kind of electrical processes occurring within the material and the correlation between the arcs and microstructure of these materials is established by an equivalent electrical circuit is shown in Fig. 5b. The experimental and theoretical fit data calculated using commercially available software (ZSIMP WIN version 2.0) for an ideal Debye-like relaxation; an equivalent circuit consists of parallel combination of (CR) and (CQR), where Q is known as constant phase element (CPE). Using the fitted curves, the values of bulk resistance (R_b), grain boundary resistance (R_{gb}), bulk capacitance (C_b) and grain boundary capacitance (C_{gb}) at different temperature were calculated, and compared in Table 1. It is observed that there is no such grain boundary effect in the material up to 200 °C which can be correlated with single RC equivalent circuit. As temperature increases from room temperature, the arc progressively becomes semicircular with a shift of the centre towards origin of the complex plane plot. On further increase in temperature, the slope of the line decreases, and bend towards Z'-axis (above 300 °C), and thus a semicircle could be traced indicating the increase in conductivity of the sample [34, 35]. The presence of semicircular arcs at temperatures above 300 °C

Table 1 Comparison of impedance fitting parameters (R_b, C_b, R_{gb}, CPE, C_{gb}) of Bi(Ni$_{0.25}$Ti$_{0.25}$Fe$_{0.50}$)O$_3$ at different temperatures

Temp.	C_b (nF)	R_b (Ω)	CPE	C_{gb} (nF)	R_{gb} (Ω)
200	2.086E−010	8.023E+5	8.566E−009	1.000E−10	4.963E+005
300	2.957E−009	1.0003E+3	8.126E−010	7.965E−011	7.248E+005
400	1.307E−009	1.000E+2	4.212E−009	8.810E−011	4.537E+004
500	3.330E−006	6.066E+1	1.833E−008	1.401E−010	2.950E+003

(up to 500 °C) suggests that the electrical processes in the material arise basically due to the contributions from bulk material (grain interior), and thus can be modelled to an equivalent electrical circuit comprising of a parallel combination of R_b and C_b. Again, decrease in R_b with rise in temperature is normally observed in semiconductors. For an ideal Debye-type relaxation, a perfect semi-circle with its center at Z' axis should be observed. But in the studied material, depressed semi-circles of non-Debye type of relaxation are observed. It also manifests that there is a distribution of relaxation time instead of a single relaxation time in the material [38, 39]. The intercept of each semi-circle on real Z' axis gives the value of bulk and grain boundary contributions in the resistance/impedance. The semi-circles in the impedance spectrum have a characteristic peak occurring at a unique relaxation frequency usually referred as resonance frequency (f_r) ($\omega_r = 2\pi f_r$). It can be expressed as $\omega_r RC = \omega_r \tau = 1$ and thus $f_r = 1/2\pi RC$, where τ is the relaxation time. The relaxation time due to bulk effect (τ_b) has been calculated using the equation $\omega_r \tau_b = 1$ or, $\tau_b = 1/2\pi f_r$.

3.4 Complex electric modulus analysis

To detect electrode polarization, grain boundary conduction effect, electrical conductivity, bulk properties and relaxation time of the ceramics, it is very much required to use complex modulus analysis technique which also provides an insight into the electrical processes occurring in the materials at various temperatures and frequencies. The following relations of electrical modulus can be used to estimate (M' and M'') as;

$$M' = A\left[\frac{(\omega RC)^2}{1+(\omega RC)^2}\right] = A\left[\frac{\omega^2\tau^2}{1+\omega^2\tau^2}\right]; \quad (2)$$

$$M'' = A\left[\frac{\omega RC}{1+(\omega RC)^2}\right] = A\left[\frac{\omega\tau}{1+\omega^2\tau^2}\right] \quad (3)$$

where symbols have their usual meaning and $A = C_0/C$.

With the use of the formalism the inhomogeneous nature of polycrystalline ceramics with bulk and grain boundary effects can easily be probed, which cannot be distinguished from complex impedance plots.

Figure 6a, b shows the variation of M' and M'' with frequency at selected temperatures 25–500 °C). The value
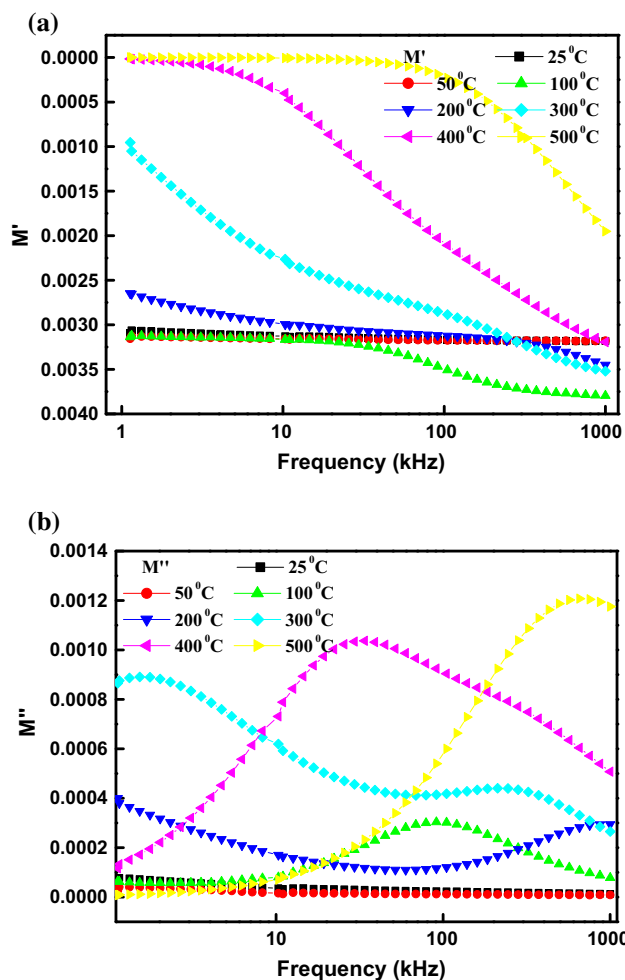

Fig. 6 a Variation of M' with frequency at selected temperatures. **b** Variation of M'' with frequency at selected temperatures

of M' approaches to zero on lowering frequency with monotonic dispersion, whereas with rise in the values of M' coincide. This may be due to presence of conduction phenomenon and short-range mobility of charge carriers. This implies that there is a lack of restoring force for flow of charges under the influence of steady electric field [40]. The M''_{max} (reaches a maximum peak) shifts to higher frequency side. This nature of dielectric relaxation suggests that the hopping mechanism of charge carriers dominates intrinsically at higher temperatures in thermally activated process. Asymmetric broadening of the peak indicates

spread of relaxation with different time constants, which suggests occurrence of non-Debye type [41].

3.5 AC conductivity studies

The ac conductivity was calculated using the dielectric data with empirical relation: $\sigma_{ac} = \omega \varepsilon_r \varepsilon_0 \tan \delta$, where ε_0 is permittivity in free space and ω is angular frequency. Detailed studies of ac conductivity are carried out for the better understanding of the frequency dependence of electrical conductivity of the material, for which we have to follow Jonscher's universal power law $\sigma_T(\omega) = \sigma(0) + \sigma_1(\omega) = \sigma_0 + a\omega^n$.

Here $\sigma(0)$ represents the frequency independent term giving dc conductivity and $\sigma_1(\omega)$ is the purely dispersive component of ac conductivity having a characteristic of power law behavior in terms of frequency (ω) [42]. The exponent n can have a value between 0 and 1, which represents the degree of interaction between mobile ions and lattices around them whereas A determines the strength of polarizibility.

Figure 7 shows the variation of σ_{ac} of the material with frequency at different temperature of $Bi(Ni_{0.25}Ti_{0.25}Fe_{0.50})O_3$. The conductivity curve shows that σ_{ac} increases with increase in frequency. The increasing trend of σ_{ac} with increase in frequency (in the low-frequency region) may be attributed to the disordering of cations between neighboring sites and presence of space charges [43]. In the high-frequency region, the curves approach each other. The nature of conductivity plots reveals that the curves exhibit low-frequency dispersion phenomena obeying Jonscher's power law [44]. According to Jonscher, the origin of the frequency dependence of conductivity lies in the relaxation phenomena arising due to mobile charge carriers. When a mobile charge carrier hops 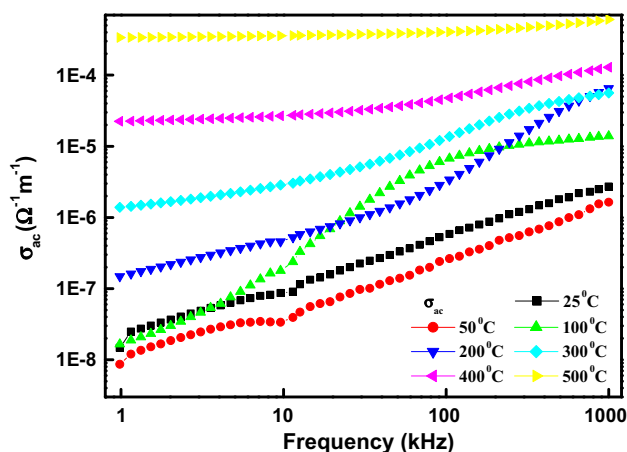to a new site from its original position, it remains in a state of displacement between two potential energy minima. Also, the conduction behavior of the materials obeys the above power law.

3.6 Magnetic study

Figure 8 shows the room temperature magnetization (M) versus applied magnetic field (H) plots of $Bi(Ni_{0.25}Ti_{0.25}Fe_{0.50})O_3$ with a maximum applied magnetic field of ± 15 kOe. The figure also indicates that the magnetic properties of BNTF are much more enhanced as compared to those of BFO. BFO has non-zero remnant magnetization (M_r) of the value of 4.72×10^{-4} emu g^{-1} at a coercive magnetic field (H_c) of 4.24×10^{-6} kOe. This is because BFO has G-type antiferromagnetic structure but the magnetic moment of Fe^{3+} cations is ferromagnetically coupled in pseudocubic (111) planes but antiferromagnetically between adjacent planes. It has a residual magnetic moment due to a canted spin structure (weak ferromagnetic) [45]. Magnetic hysteresis-loop for modified BFO ceramics shows the linear magnetic field dependence of magnetization which indicates that it is antiferromagnetic material. The value of remnant magnetization (M_r), saturation magnetization (M_s) and coercive field (H_c) is 0.038424 emu g^{-1}, 0.13156 emu g^{-1} and 298.98 Oe respectively. These values are found to be much better as compared to those of some known multiferroics, such as $BiFeO_3$, $Bi_{1-x}Ho_xFeO_3$ (x = 0.15 and x = 0.20) [46–48]. The value of magnetic moment corresponding to the saturation magnetization is 0.01779 emu. The enhanced values of magnetization may be due to both A and/or B site doping. However, the simultaneous substitution of Ni and Ti into $BiFeO_3$ induces high ferromagnetism which is
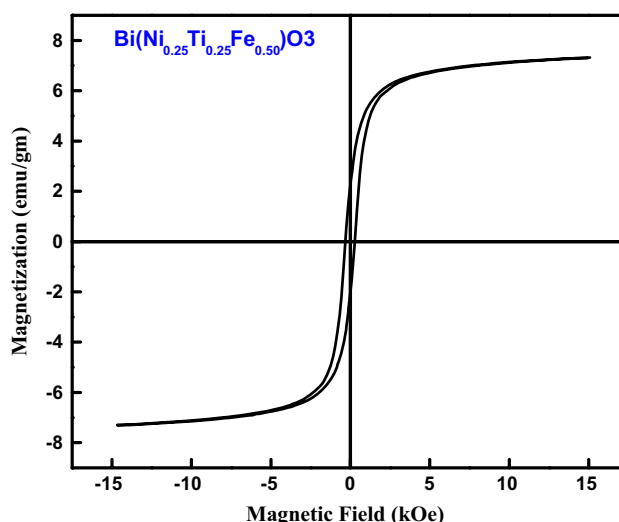

Fig. 7 Variation of ac conductivity with frequency at different temperature of $Bi(Ni_{0.25}Ti_{0.25}Fe_{0.50})O_3$

Fig. 8 Magnetic hysteresis loop of $Bi(Ni_{0.25}Ti_{0.25}Fe_{0.50})O_3$ at room temperature

evident from the enhancement in remnant magnetization and coactivity for the co-substituted BFO ceramics. The unsaturated hysteresis loops and presence of high remnant magnetization indicates the signature of high ferromagnetism.

4 Conclusion

The polycrystalline samples of $Bi(Ni_{0.25}Ti_{0.25}Fe_{0.50})O_3$ was synthesized using a standard high-temperature solid-state reaction technique. Preliminary structural study suggests that structural change was observed with the substitution of (Ni, Ti) at the Fe site of BFO. The R_b decreases on substituting the concentration of the co-substitution. The impedance studies exhibit the presence of grain (bulk) and grain boundary effects, and existence of a negative temperature coefficient of resistance (NTCR) in the material. Modulus analysis indicates that the material obey the non-exponential type of conductivity relaxation. The experimental observations of impedance studies were used to estimate the electrical conductivity of the material. We used an equivalent circuit to demonstrate electrical phenomena occurring inside the material. There is a significant enhancement in the remnant magnetization for BNTF which increase further on substitution of percentage. It leads to the increase of the M_r due to appearance of complete antiferromagnetic ordering. The enhanced magnetic properties will be interesting for magnetic field sensor applications.

References

1. W. Eerenstein, N.D. Mathur, J.F. Scott, Nature 442, 759 (2006)
2. G. Catalan, J.F. Scott, Adv. Mater. 21, 2463–2485 (2009)
3. S.W. Cheong, M. Mostovoy, Nat. Mater. 6, 13–20 (2007)
4. R. Ramesh, N.A. Spaldin, Nat. Mater. 6, 21–29 (2007)
5. A. Singh, V. Pandey, R.K. Kotnala, D. Pandey, Phys. Rev. Lett. 101, 247602 (2008)
6. A.M. Glazer, Acta Crystallogr. Sect. A 31, 756 (1975)
7. C.W. Nan, M.I. Bichurin, S. Dongb, D. Viehland, J. Appl. Phys. 103, 031101 (2008)
8. Y.P. Wang, L. Zhou, M.F. Zhang, X.Y. Chen, J.M. Liu, Z.G. Liu, Appl. Phys. Lett. 84, 1731–1733 (2004)
9. V.R. Palkar, J. John, R. Pinto, Appl. Phys. Lett. 80, 1628 (2002)
10. Y. Shimizu, K. Uemura, N. Miura, N. Yamzoe, Chem. Lett. 17, 1979–1982 (1988)
11. T. Cao, Y. Li, C. Wang, C. Shao, Y. Liu, Langmuir 27, 2946–2952 (2011)
12. B. Zielinska, E. Borowiak-Palen, R.J. Kalenczuk, Int. J. Hydrogen Energy 33, 1797–1802 (2008)
13. X. Lin, J. Xing, W. Wang, Z. Shan, F. Xu, F. Huang, J. Phys. Chem. C 111, 18288–18293 (2007)
14. M.I. Petrov, D.A. Balaev, K.A. Shaihutdinov, K.S. Aleksandrov, Phys. C 341, 1863–1864 (2000)
15. H. Wendt, G. Imarisio, J. Appl. Electrochem. 118, 1–14 (1988)
16. R.P. Liferovich, R.H. Mitchell, Phys. Chem. Miner. 32, 442–449 (2005)
17. S.N.S. Reddy, D.N. Leonard, L.B. Wiggins, K.T. Jacob, Metall. Mater. Trans. A Phys. Metall. Mater. Sci. 36, 2685 (2005)
18. P.S. Anjana, M.T. Sebastianw, J. Am. Ceram. Soc. 89, 2114 (2006)
19. Y.M. Chiang III, D. Birnie, W.D. Kingery, Physical ceramics, vol. 34 (Wiley, New York, 1996)
20. R. Palai, R.S. Katiyar, H. Schmid, P. Tissot, S.J. Clark, J. Robertson, S.A.T. Redfern, G. Catalan, J.F. Scott, Phys. Rev. B 77, 014110 (2008)
21. E. Wu, An interactive powder diffraction data interpretations and indexing Program Version 2.1, School of Physical Sciences, Flinders University of South Australia, SA 5042 (1989)
22. B.D. Cullity, Elements of X-ray diffraction, 2nd edn. (Addison-Wesley, Bosten, 1978)
23. M. Panahi-Kalamuei, P. Rajabpour, M. Salavati-Niasari, Z. Zarghami, M. Mousavi-Kamazani, J. Mater. Sci. Mater. Electron. 26, 3691–3699 (2015)
24. A. Sobhani, M. Salavati-Niasari, J. Mater. Sci. Mater. Electron. 26, 6831–6836 (2015)
25. I.V. Kityk, M. Makowska-Janusik, M.D. Fontana, M. Aillerie, A. Fahmi, J. Phys. Chem. B 105, 12242 (2001)
26. I.V. Kityk, M. Makowska-Janusik, M.D. Fontana, M. Aillerie, A. Fahmi, J. Appl. Phys. 90, 5542 (2001)
27. K. Jawahar, R.N.P. Choudhary, Mater. Lett. 62, 911 (2008)
28. J.C. Anderson, Dielectrics (Chapman & Hall, London, 1964)
29. S. Sen, R.N.P. Choudhary, Mater. Chem. Phys. 87, 256 (2004)
30. S. Brahma, R.N.P. Choudhary, A.K. Thakur, Phys. B 355, 188 (2005)
31. J.R. Macdonald, Impedance spectroscopy emphasizing solid materials and systems (Wiley, New York, 1987)
32. J. Suchanicz, Mater. Sci. Eng. B 55, 114 (1998)
33. C.K. Suman, K. Prasad, R.N.P. Choudhary, J. Mater. Sci. 41, 369 (2006)
34. V. Provenzano, L.P. Boesch, V. Volterra, C.T. Moynihan, P.B. Macedo, J. Am. Ceram. Soc. 55, 492 (1972)
35. H. Jain, C.H. Hsieh, J. Non-Cryst, Solids 172, 1408 (1994)
36. S. Chatterjee, P.K. Mahapatra, R.N.P. Choudhary, A.K. Thakur, Phys. Status Solidi 201, 588 (2004)
37. S. Pattanayak, B.N. Parida, P.R. Das, R.N.P. Choudhary, Appl. Phys. A 112, 387–395 (2013)
38. S. Sen, R.N.P. Choudhary, P. Pramanik, Phys. B 387, 56 (2007)
39. B. Behera, P. Nayak, R.N.P. Choudhary, J. Alloys Compd. 436, 226 (2007)
40. I.M. Hodge, M.D. Ingram, A.R. West, J. Electroanal. Chem. 58, 429 (1975)
41. J.R. Macdonald, Solid State Ion. 13, 147 (1984)
42. D.C. Sinclair, A.R. West, J. Appl. Phys. 66, 3850 (1989)
43. N.K. Karan, D.K. Pradhan, R. Thomas, B. Natesan, R.S. Katiyar, Solid State Ion. 179, 689 (2008)
44. A.K. Jonscher, Nature 267, 673 (1977)
45. A. Mishra, S.N. Choudhary, R.N.P. Choudhary, V.R.K. Murthy, K. Prasad, J. Mater. Sci. Mater. Electron. 23, 185–192 (2012)
46. N. Van Minh, N. Gia Quan, J. Alloys Compd. 509, 2663–2666 (2011)
47. P. Guzdek, J. Magn. Magn. Mater. 349, 219–223 (2014)
48. H.O. Rodrigues, G.F.M.P. Junior, J.S. Almeida, E.O. Sancho, A.C. Ferreira, M.A.S. Silva, A.S.B. Sombra, J. Phys. Chem. Solids 71, 1329–1336 (2010)